Gong, Qianhong; Yang, Dawei; Yang, Huiping; [et al.]. «Cobalt Ditelluride Meets Tellurium Vacancy : An Efficient Catalyst as a Multifunctional Polysulfide Mediator toward Robust Lithium-Sulfur Batteries». ACS Nano, Vol. 18, Issue 41 (October 2024), p. 28382-28393. DOI 10.1021/acsnano.4c11068

Cobalt Ditelluride Meets Tellurium Vacancy: An Efficient Catalysts as Multifunctional Polysulfide Mediator toward Robust Lithium-Sulfur Batteries

Qianhong Gong,[†] *Dawei Yang,*[*,†,‡] *Huiping Yang,*[§] *Konglin Wu,*[∆] *Jie Zhang,*[†] *Wei Bi,*[†] *Jiefeng Diao,*[*,◊] *Canhuang Li,*[‡] *Jing Yu,*[‡,//] *Chao Yue Zhang,*[‡] *Mengyao Li,*[&] *Graeme Henkelman,*[◊] *Jordi Arbiol,*[§,//,$] *Qiaobao Zhang,*[*,§,±] *Andreu Cabot*[*,‡,$]

[†] Henan Key Laboratory of Quantum Materials and Quantum Energy, School of Quantum Information Future Technology, Henan University, Kaifeng, 475004, China.

[‡] Catalonia Institute for Energy Research - IREC, Sant Adrià de Besòs, Barcelona, 08930, Spain.

[∆] Carbon Cycle and Emission Control Research Center of Low-Carbon Research Institute, Institute of Clean Energy and Advanced Nanocatalysis, School of Chemistry and Chemical Engineering, Anhui University of Technology, Maanshan, 243002, China.

[◊] Department of Chemistry and the Oden Institute for Computational Engineering and Sciences, The University of Texas at Austin, Austin, TX, 78712 USA.

[&] School of Physics and Microelectronics, Zhengzhou University, Zhengzhou 450052, P. R. China.

[§] State Key Laboratory of Physical Chemistry of Solid Surfaces, College of Materials, Xiamen University, Xiamen, Fujian, 361005 China

[±] Longmen Laboratory, Luoyang 471023, Henan, China

[//] Catalan Institute of Nanoscience and Nanotechnology (ICN2), CSIC and BIST, Campus UAB, Bellaterra, 08193 Barcelona, Spain.

[$] ICREA, Pg. Lluís Companys 23, 08010 Barcelona, Spain.

Email: dwyang@henu.edu.cn

Email: diaojf@utexas.edu

Email: zhangqiaobao@xmu.edu.cn

Email: acabot@irec.cat

Abstract

The commercialization of lithium-sulfur batteries (LSBs) faces significant challenges due to persistent issues such as the shuttle effect of lithium polysulfides (LiPS) and the slow kinetics of cathodic reactions. To address these limitations, this study proposes a vacancy-engineered cobalt ditelluride catalyst (v-$CoTe_2$) supported on nitrogen-doped carbon as sulfur host at the cathode. Density functional theory (DFT) calculations and experimental results indicate that the electron configuration modulation of v-$CoTe_2$ enhances the chemical affinity and catalytic activity towards LiPS. Specifically, v-$CoTe_2$ can strongly interact with polysulfides through multi-site coordination, effectively facilitating the kinetics of the LiPS redox reaction. Furthermore, the introduction of Te vacancies generates a large number of spin-polarized electrons, further enhancing the reaction kinetics of LiPS. As a result, the v-$CoTe_2$@S cathode demonstrates high initial capacity and excellent cyclic stability, maintaining 80.4% capacity after 500 cycles at a high current rate of 3 C. Even under a high sulfur load of 6.7 mg cm^{-2}, a high areal capacity of 6.1 mAh cm^{-2} is retained after 50 cycles. These findings highlight the significant potential of Te vacancies in $CoTe_2$ as sulfur host material for LSBs.

Keywords: Tellurium vacancies, cobalt ditelluride, lithium polysulfides, catalytic conversion, lithium-sulfur batteries

Lithium-sulfur batteries (LSBs) have been recognized as a promising candidate for the next generation energy-storage systems owing to its outstanding theoretical specific capacity and energy density, the low cost/abundance of sulfur, and the environmentally friendly components and process.[1-3] However, several persistent limitations such as the electrically insulating nature of the final discharge/charge products (S and Li_2S_2/Li_2S),[4] the dissolution and migration of the intermediate LiPS in the commonly used electrolytes, known as the shuttle effect,[5] and the volume expansion restrain the commercialization of LSBs.[6] All those barriers result in the loss of sulfur, the reduction of Coulombic efficiency and the degradation of cell capacity.[7] From the reaction and failure mechanism of LSBs, it can be inferred that enhancing the adsorption of LiPS can lead to a longer lifespan and higher capacity.[8, 9]

Recently, various sulfur hosts and additives, including carbonaceous materials,[10-12] metal oxides[13, 14] and transition metal chalcogenides (TMCs),[15, 16] have been extensively investigated for LSBs. Among them, TMCs show much stronger bonding with polysulfide and higher catalytic activity than carbon materials due to the polar-polar interaction.[17, 18] Compared with transition metal sulfides and selenides, transition metal tellurides (TMTs) exhibit higher electrical conductivity, high catalytic activities related to the metal cation and similar polarities.[19] Stoichiometric cobalt ditelluride ($CoTe_2$) presents a relatively high degree of covalency in the metal-anion bonding, which provides it with metallic conductivity, but moderate catalytic activity.[20-23]

Although some progress has been made in the application of TMCs in LSBs, it is still a challenge to suppress the shuttle effect effectively and boost the kinetics of electrochemical reactions.[24] Vacancy engineering has been proven a feasible strategy to tune the electronic structures of metallic compounds thus adjusting their adsorption and electrocatalytic properties.[25, 26] The introduction of anionic vacancies can bring more active sites and charge carriers to the material, thereby improving conductivity to enhance the sulfur utilization.[27] In addition, it is worth noting that the presence of vacancies increases the number of unpaired electrons, which may lead to changes in the electron spin state, thus enhancing the overall magnetization and generating a large number of potential spin-polarized electrons that can accelerate the Li-S reaction kinetics.[28-31]

Herein, vacancy-engineered cobalt ditelluride electrocatalysts (v-$CoTe_2$) are produced and explored as sulfur hosts in LSBs. The electronic configurations modulation of v-$CoTe_2$ with polyhedral architecture expose abundant active sites and strengthen the chemical affinity to LiPS. Besides, spin polarization induced by tellurium vacancies lowers the reaction barrier, thereby exhibiting enhanced catalytic ability, and accelerating the reaction kinetics of LiPS conversion. Therefore, LSBs based on v-$CoTe_2$@S cathodes display more stable cycling performance and superior rate capability. Moreover, stable cycling under the conditions of high sulfur loading with lean electrolyte is demonstrated, further validating the practical application potential of v-$CoTe_2$.

Results and Discussion

DFT calculations were used first to determine the $CoTe_2$ and v-$CoTe_2$ configurations, band structures and surface charge distributions at the atomic scale. After geometry optimization, we observe the introduction of surface Te vacancies to result in a surface reconstruction as shown in Figure 1a, v-$CoTe_2$ can strongly interact with polysulfides like Li_2S_4 through multi-site coordination (Figure 1b). This is explained by the increase in the d-band centre of surface Co atoms (-0.539 eV for $CoTe_2$, -0.452 eV for v-$CoTe_2$). The stronger interaction associated with the presence of Te vacancies leads to a high filling fraction of the Li_2S_4 lowest occupied molecular orbital (LUMO), which not only results in high adsorption energy but also facilitates polysulfide decomposition by weakening the S-S bond. Comparing the surface configurations of $CoTe_2$ and v-$CoTe_2$, we can see that with the surface reconstruction, more Te atoms are directly exposed on the surface. Interestingly, the changes in surface geometric configurations are associated with charge rearrangements (Figure 1c). The charge transfer diagram clearly shows that for the v-$CoTe_2$ surface, a large amount of electrons are transferred from Co atoms to Te atoms, resulting in a higher electronic spin state in Co. Bader charge calculated the charge distribution on each surface atom (Figure 1d). Overall the surface layer of v-$CoTe_2$ gains 0.353 electrons (per unit cell) from the layers underneath; and the surface Co atoms lose 0.968 electrons while Te atoms gain 1.321 electrons. This charge redistribution appears to be significantly larger than that of the $CoTe_2$ surface, with Co atoms losing 0.111 electrons and Te atoms gaining 0.309 electrons. Taking advantage of the electronic rearrangements, it is easier for polysulfides to adsorb on the surface with multiple coordination. Besides, v-$CoTe_2$ also appears to have more electrons around the Fermi surface (Figure 1e). All these results explain the higher adsorption energies on v-$CoTe_2$ compared to $CoTe_2$. As schematized in Figure 1f, the stronger multi-site coordination adsorption of polysulfides on the v-$CoTe_2$ surface should significantly block the migration effect of polysulfides from cathode to anode and simultaneously accelerate their conversion, particularly the conversion from insoluble Li_2S_6 to soluble Li_2S.

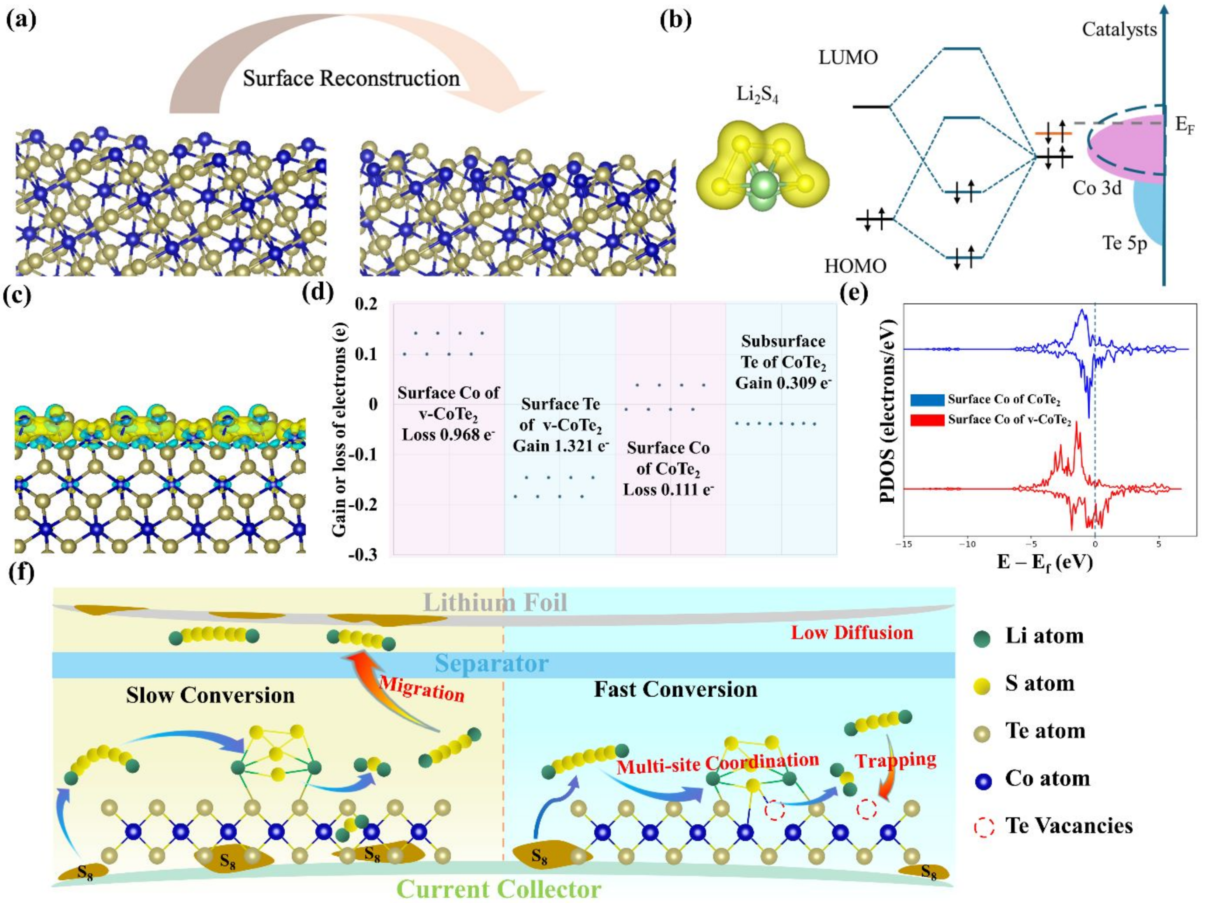

Figure 1. (a) Surface structures of $CoTe_2$ (left) and v-$CoTe_2$ (right). (b) Scheme of orbital interactions between polysulfides and $CoTe_2$/v-$CoTe_2$. (c) Charge transfer diagram of v-$CoTe_2$ after surface reconstruction (yellow and blue isosurfaces indicate the gain and loss of electrons). (d) Bader charge analysis of the different surface atoms. (e) Density of states of surface Co atoms for $CoTe_2$/v-$CoTe_2$. (f) Schematic illustrations of the multi-site coordination mechanism of LiPSs on the matrix of $CoTe_2$ (left) and v-$CoTe_2$(right).

The schematic illustration of the preparation process of v-$CoTe_2$ is shown in Figure 2a. First, the Co-ZIF-67 precursor with polyhedron-shaped structure was prepared by the coordination reaction between the transition-metal-ion precursor ($Co(NO_3)_2 \cdot 6H_2O$) and 2-methylimidazole in methanol. Afterwards, the obtained ZIF powder was reacted with tellurium powder in an Ar-filled tube furnace to produce a composite powder made of carbon and $CoTe_2$ particles.[16] Subsequently, Te vacancies were generated by annealing the powder in a reducing atmosphere (Ar/H_2).[32]

The architecture of the v-$CoTe_2$ based composite and its precursor materials was characterized by transmission electron microscopy (TEM) and scanning electron microscopy (SEM). SEM images of ZIF-67 and v-$CoTe_2$ are displayed in Figure 2b,c and S1. The precursor ZIF-67 has a smooth surface and shows a typical polyhedral shape with the size of 200-300 nm. The v-$CoTe_2$ obtained after tellurization and annealing in a reducing atmosphere maintained the morphology of ZIF-67 but presented a rougher surface (Figure 2c).[33] v-$CoTe_2$ appears to be formed by a porous dodecahedral polyhedron carbon matrix loaded with nanoparticles of about 20 nm (Figure 2d**).** EDS and EELS elements mapping confirmed the homogeneous distributions of Co, Te, C, and N elements on the v-$CoTe_2$ polyhedron (Figure 2e and S2). The crystal structures of v-$CoTe_2$ and $CoTe_2$ were verified by HRTEM and XRD characterization in Figure 2f and g. All the diffraction peaks were indexed to the orthorhombic $CoTe_2$ (JCPDS No.74-0245), respectively.[34] Small peak upshifts about 0.1° was observed in the magnified XRD pattern (Figure S3), indicating the gradually decreased lattice parameters in v-$CoTe_2$.[35] Also the magnified XRD pattern shows the peak shift of v-$CoTe_2$, which may attribute to the changed Te-Co-Te bond distance induced by the Te vacancies.[20, 36] Meanwhile, the HRTEM image in Figure 2f shows a lattice distance of 0.28 nm that can be attributed to the (111) plane of orthorhombic $CoTe_2$, consistently with XRD data.

The electron paramagnetic resonance (EPR) spectrum of v-$CoTe_2$ showed a sharp signal peak at g=2.003 not obtained for the $CoTe_2$ sample. This signal is associated with unpaired electron spins associated with the presence of Te vacancies generated during annealing under the reducing (Ar/H_2) atmosphere (Figure 2h). Besides, v-$CoTe_2$ exhibited a relatively high electrical conductivity, 518.6 S cm^{-1}, well above that of $CoTe_2$, 351.2 S cm^{-1}, as measured via the four-point probe characterization .

X-ray photoelectron spectroscopy (XPS) was applied to determine the composition and valence state of each element of v-$CoTe_2$ and $CoTe_2$. The analysis results illustrated the presence of N, C, O, Co, and Te in both samples (Figure S4a). The Co 2p XPS spectrum of v- $CoTe_2$ (Figure 2h) exhibited one doublet at 780.5 eV (Co $2p_{3/2}$) and 796.4 eV (Co $2p_{1/2}$) associated with Co^{2+}.[37] These binding energies are redshifted compared with $CoTe_2$ (780.8 and 796.7 eV). The other two observed peaks in the Co 2p spectra are assigned to satellite bands.[38] The Te 3d XPS spectrum of $CoTe_2$ displayed the doublet at 573.1 and 583.5 eV that can be assigned to Te within the $CoTe_2$ lattice, while the doublet at 575.9 and 586.4 eV is assigned to a surface oxidised Te-O component generated during air exposure of the sample prior to XPS analysis (Figure 2i).[20, 32, 39] Furthermore, a slight negative shift of the Te 3d spectrum was also observed for v-$CoTe_2$ when compared with $CoTe_2$. The high-resolution C 1s spectrum (Figure S4b) of v-$CoTe_2$ exhibits four peaks attributed to C-C, C-N, C-O and C=O, respectively. The N 1s spectrum (Figure S4c) displays three peaks at the binding energy of 389.6, 399.8 and 402.1 eV, corresponding to pyridinic-N, pyrrolic-N and graphitic-N respectively.[9, 40] Pyridine nitrogen and graphitic nitrogen have little effect on the carbonaceous-structure because the bond length of C-N (1.41 Å) is similar to C-C (1.42 Å).[41, 42] However, pyrrolic N disrupts the six-atomic ring structure of graphitic carbon. Therefore, the existence of the three types of nitrogen is accompanied by structural defects in the carbonaceous material and non-cyclic structure leading to disordered structures, thus exposing more active sites, and potentially increasing electron density and interaction with sulfur/polysulfide.[43, 44]

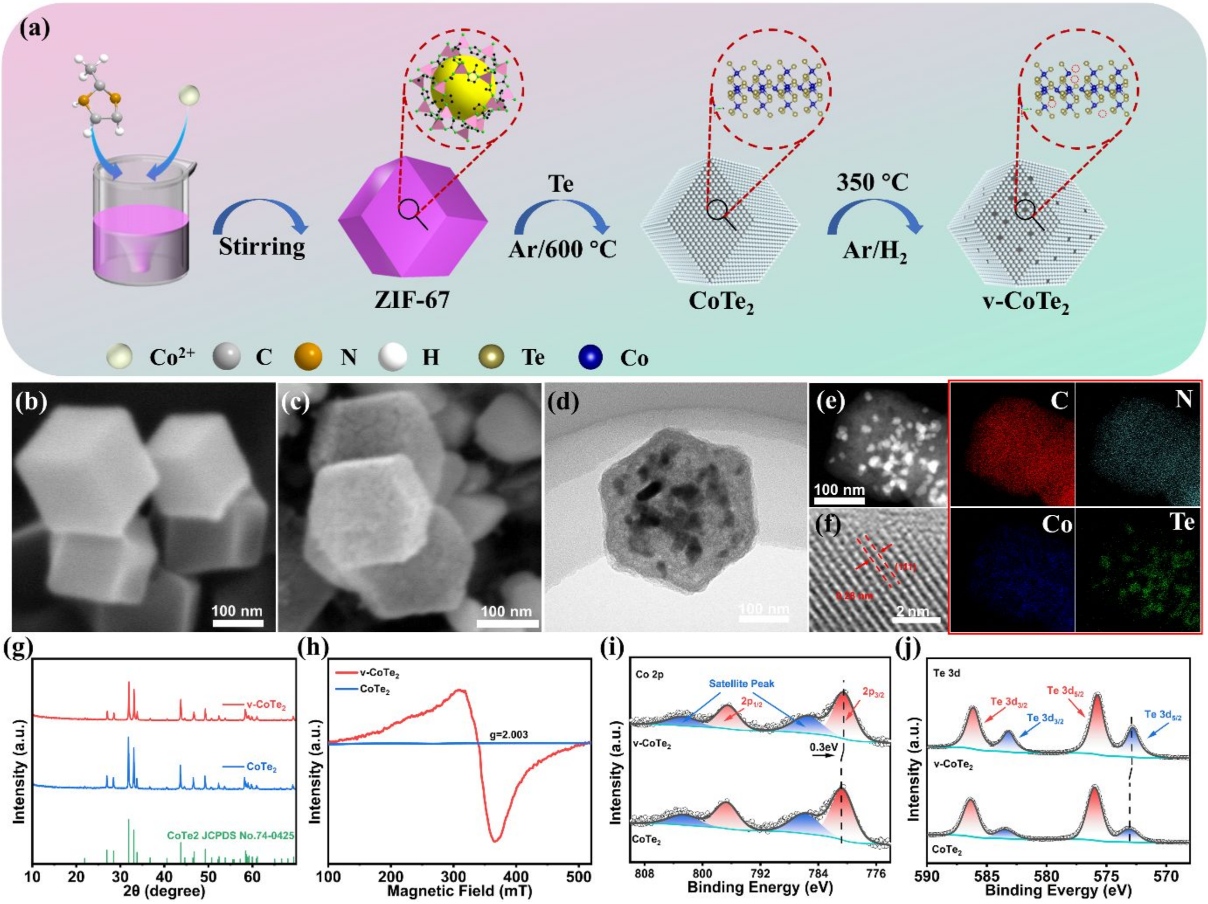

Figure 2. (a) Schematic illustration of the production of $CoTe_2$ and v-$CoTe_2$. (b) SEM image of ZIF-67. (c) SEM image of v-$CoTe_2$. (d) TEM image of v-$CoTe_2$. (e) TEM-EDS mapping images of v-$CoTe_2$.(f) HRTEM image of v-$CoTe_2$. (g) XRD pattern of v-$CoTe_2$ and $CoTe_2$. (h) EPR spectra of the v-$CoTe_2$ and $CoTe_2$. (i) Co 2p XPS spectra and (j) Te 3d XPS spectra of v-$CoTe_2$ and $CoTe_2$.

To determine the adsorption ability of different compounds with LiPS, the Li_2S_6 adsorption experiment was carried out. Equal mass of v-$CoTe_2$ and the reference materials $CoTe_2$ and

Super P, were introduced into Li_2S_6 solutions and left undisturbed overnight. After this time, obvious differences in the solution colour, assigned to the concentration of Li_2S_6, can be observed in the optical photographs (inset of Figure 3a). The Li_2S_6 solution containing v-$CoTe_2$ showed a much paler colour than the solution with $CoTe_2$ and Super P. This lightened colour indicates more effective adsorption of Li_2S_6. The Li_2S_6 absorption test was further confirmed by UV-vis spectroscopy (Figure 3a). The absorbance of the four Li_2S_6 solutions in the region of 350-400 nm is significantly different, corresponding to the adsorption ability of different materials shown in Figure 3a.[45, 46]

The high-resolution Co 2p and N 1s XPS spectra after and before the Li_2S_6 adsorption test are shown in Figure 3b and c. After the adsorption of Li_2S_6, the peaks of Co 2p shifted to a lower binding energy, associating with the Co interaction with the more electronegative S atom that leads to a higher electron density of Co 2p.[47] Besides, when Li_2S_6 is adsorbed on v-$CoTe_2$, a clear blueshift was observed in the N 1s bands related to a higher electronegativity environment that we attribute this phenomenon to the interaction between Li and N. This result indicates that the N doping improves the interaction with LiPSs and that overall, v-$CoTe_2$ exhibits a dual-anchoring mechanism to trap LiPS.[48]

Additional DFT calculations were futher investigated to gain insight into the interaction of the host materials with LiPS. The optimized surface adsorption configurations of LiPS at six different lithiation stages on $CoTe_2$ and v-$CoTe_2$ surfaces are shown in Figure S5 and S6. The calculation results confirmed that v-$CoTe_2$ displayed multi-site coordination with LiPS, which endows it with a strong interaction with LiPS. Figure 3d displays the configurations of Li_2S_6 on v-$CoTe_2$ and $CoTe_2$, and the calculated binding energy (E_b) for Li_2S_6 anchored on v-$CoTe_2$ and

$CoTe_2$ surface to be -5.92 and -5.80 eV. Figure 3e presents the E_b of the different LiPS adsorbed on the surfaces of v-$CoTe_2$ and $CoTe_2$. Overall, the consistent experimental results and DFT calculations proved a high affinity of v-$CoTe_2$ toward LiPSs, associated with the multiple and effective LiPS coordination sites on the v-$CoTe_2$ surface.[49]

The redox kinetics of LiPS were further studied by DFT calculation. The three states of Li_2S decomposition on $CoTe_2$ and v-$CoTe_2$ are exhibied in Figure S7. v-$CoTe_2$ showed a significantly lower Li_2S decomposition energy barrier (0.26 eV) than $CoTe_2$ (0.35 eV). Besides, the Li-ion diffusion energy barriers ($E_{barrier}$) in different states on the surface of $CoTe_2$ and v-$CoTe_2$ are displayed in Figure 3f. The calculated $E_{barrier}$ for v-$CoTe_2$ was only 0.20 eV, which is considerably smaller than that of $CoTe_2$ (0.28 eV). The calculated results indicate the presence of Te vacancies to have associated enhanced LiPS redox kinetics and catalytic activity. Besides, the Gibbs free energies of discharge intermediates and their optimized structures on the surfaces of $CoTe_2$ and v-$CoTe_2$ are shown in Figure 3g. The reduction process from Li_2S_2 to Li_2S contributes half of the capacity in the discharge process of LSBs. Generally speaking, the largest increase in Gibbs free energy (ΔE) from Li_2S_2 to Li_2S is considered the decisive step for the evaluation of electrocatalytic activity.[50] The much lower ΔE of v-$CoTe_2$ (1.17 eV) compared with $CoTe_2$ (2.49 eV) indicates that the presence of Te vacancies in v-$CoTe_2$ can catalyze LiPS more effectively, which should translate into an enhancement of the electrochemical performance of LSBs.

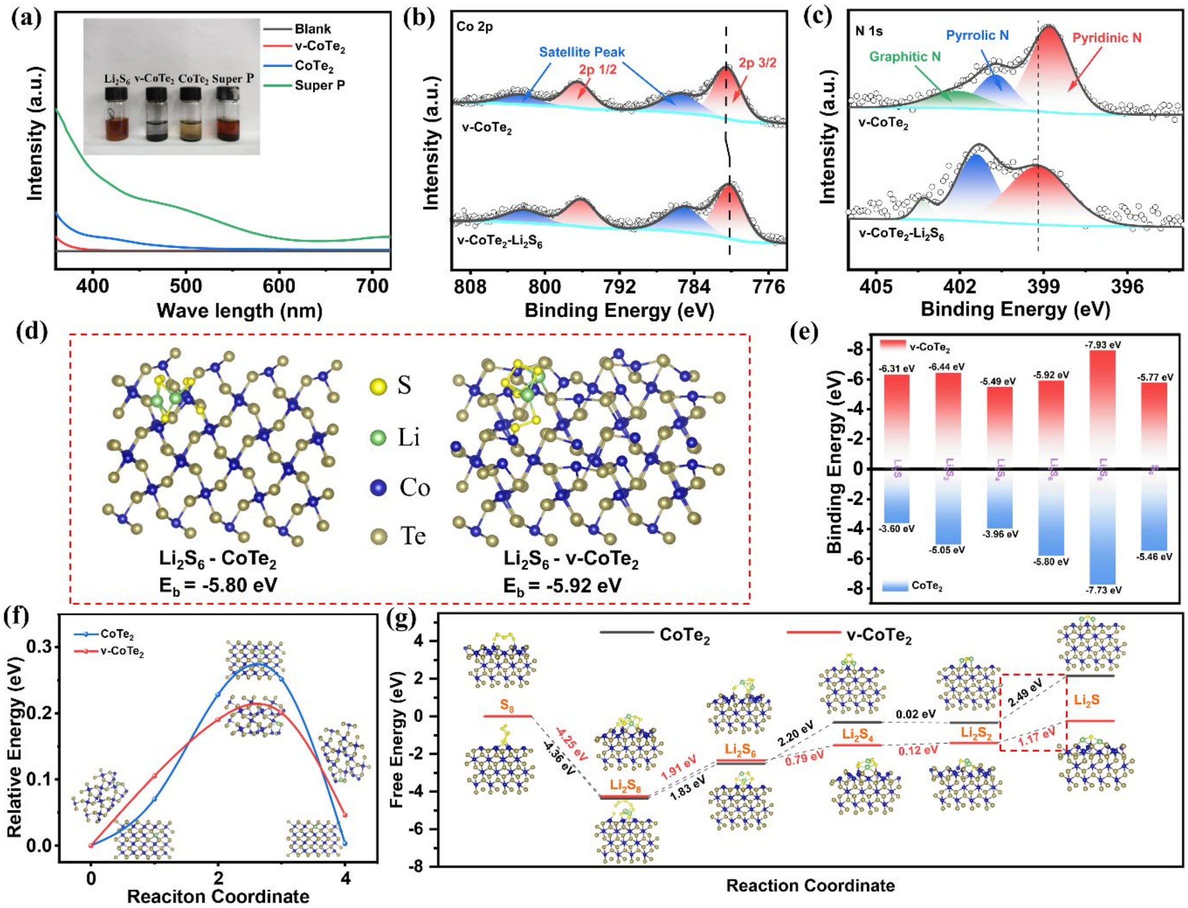

Figure 3. (a) UV-vis spectrum of polysulfide solution mixed with different adsorbents overnight. Inset shows an optical photograph of Li_2S_6 solutions containing (from left to right: Li_2S_6 solution, v-$CoTe_2$, $CoTe_2$, Super P). (b, c) High-resolution XPS of the Co 2p and N 1s spectra of v-$CoTe_2$ after and before the adsorption of Li_2S_6. (d) Adsorption configurations for Li_2S_6 on a $CoTe_2$ (left) and v-$CoTe_2$ (right) surfaces. (e) Binding energy between $CoTe_2$, v-$CoTe_2$ and LiPS species. (f) Energy profile of Li^+ diffusion on $CoTe_2$ and v-$CoTe_2$ surfaces. (g) Gibbs free energy diagrams and the optimized adsorption configurations of LiPS species on v-$CoTe_2$ and $CoTe_2$.

The electrocatalytic activity was experimentally analyzed by measuring CV curves on symmetric cells. The symmetric cells were assembled with the three catalysts in both electrodes without sulfur. As shown in Figure 4a, the v-$CoTe_2$ symmetric cell displayed the highest current peak, while the CV curves of $CoTe_2$ and particularly Super P symmetric cells exhibited much lower current densities, suggesting that $CoTe_2$ and especially the presence of Te vacancies within the telluride significantly promote the redox conversion kinetics of polysulfides.

Sulfur was introduced by a melt infiltration process. XRD patterns (Figure S8) of the v-$CoTe_2$@S composite display the peaks of cubic sulfur (JCPDS No.08-0247) and orthorhombic $CoTe_2$ (JCPDS No.74-0245).[51] The content of sulfur in the composite was detected by thermogravimetric analysis (TGA) at about 72% (Figure S9). As observed from SEM analysis (Figure S10a, b), the polyhedral particle architecture was well inherited by v-$CoTe_2$ after sulfur loading. The presence of sulfur in the composite was further confirmed by nitrogen adsorption-desorption isotherms of the v-$CoTe_2$@S and v-$CoTe_2$ (Figure S11a, b). The Brunauer–Emmett–Teller (BET) analysis showed the specific surface area of v-$CoTe_2$ was 98 $m^2\ g^{-1}$, and it decreased to 0.9 $m^2\ g^{-1}$ after the sulfur incorporation. Meanwhile, due to the incorporation of sulfur, the pore volume of v-$CoTe_2$@S was reduced to 0.02 $cm^3\ g^{-1}$.

Figure 4b showed the CV curve of coin cells based on the different cathode materials (v-$CoTe_2$@S, $CoTe_2$@S, Super P@S) and Li foil as anode (see details in the SI). All curves exhibit two cathodic peaks (peak I and peak II) corresponding to the reduction of S_8. The single anodic peak (peak III) was related to the oxidation of polysulfides to S_8.[9, 52] As shown in Figure 4b, the v-$CoTe_2$@S composite exhibited more positive peak potentials and more negative peak potentials than the other electrodes.

To quantitatively estimate the catalytic activity, onset potentials (OPs) were defined as the potential at a current density of 10 $\mu A\ cm^{-2}$ beyond the baseline current.[53] Cells based on v-$CoTe_2$@S cathodes showed higher OPs of cathodic peaks and lower OPs of anodic peaks than the cells with the reference cathodes (Figure 4d and S12). Besides, the cells with v-$CoTe_2$@S cathodes exhibited a much smaller Tafel slope during the charge/diacharge process in Figure

4c and S13 (36 mV dec^{-1} and 58 mV dec^{-1}), indicating faster reaction kinetics in the presence of Te vacancies.

CV curves at various scan rates were measured to evaluate the Li diffusion properties of the prepared cathodes. As shown in Figure 4e and S14, the peak current increased with the increase in scan rate, but the preservation of the CV shape confirmed the electrochemical stability of v-$CoTe_2$. Moreover, the CV curve displayed a linear relationship between the peak currents (peak I, peak II and peak III) and the square root of the scan rate, denoting a diffusion-controlled process (Figure 4f and S15). Thus the Li^+ diffusion constant was calculated by the Randles-Sevcik formula:[54]

$$I_p=(2.69\times10^5)n^{1.5}AD_{Li+}{}^{0.5}C_{Li+}v^{0.5} \quad (1)$$

where the I_p stands for the peak current, n stands for the number of charge transfer, A stands for the electrode area, C_{Li+} stands for the concentration of Li^+ in the electrolyte, and ν stands for the scan rate. According to this formula, the v-$CoTe_2$ exhibited the highest Li^+ diffusion when considering both the cathodic and anodic peaks, 3.26×10^{-7}, 4.47×10^{-7}, 6.35×10^{-7} cm^2 s^{-1}, respectively. The improved lithium-ion diffusivity is related to a combination of two main factors: i) the higher catalytic activity could reduce the electron transfer barrier; and ii) the stronger binding energy with polysulfide reduces the electrolyte viscosity.[16]

The catalytic properties of the cathode materials were further assessed by analyzing the Li_2S nucleation process. From the nucleation processes (see details in the SI), we observe that the time required to reach the peak current for the v-$CoTe_2$ cathode is the shortest (Figure 4g). This cathode also provides the highest discharge peak during the potentiostatic measurement. According to Faraday's law, the Li_2S deposition capacity of v-$CoTe_2$ was 104.52 mAh g^{-}

higher than that of $CoTe_2$ (80.41 mAh g^{-1}) and Super P (50.56 mAh g^{-1}). These results demonstrate that the introduction of Te vacancies not only significantly improved the transformation of polysulfides but also promoted the nucleation reaction of Li_2S which is a key step in the sulfur lithiation process.[22]

To further investigate the electrocatalysis performance of the different materials, galvanostatic charge/discharge (GCD) curves at 0.1 C were measured (Figure 4h). The galvanostatic discharge curves present two discharge plateaus related to the conversion between sulfur and long-chain LiPS ($S_8 \rightarrow S_6^{2-} \rightarrow S_4^{2-}$) and the further reduction to Li_2S ($S_4^{2-} \rightarrow Li_2S_2 \rightarrow Li_2S$). In contrast, the charge curves exhibited one charge plateau related to the oxidation of Li_2S to S_8. The voltage difference (ΔE) between the charge/discharge plateaus at 50% discharge capacity is defined as the polarization potential.[55] The v-$CoTe_2$@S showed a lower value of ΔE than $CoTe_2$@S and Super P@S electrodes as exhibited in Figure 4i.

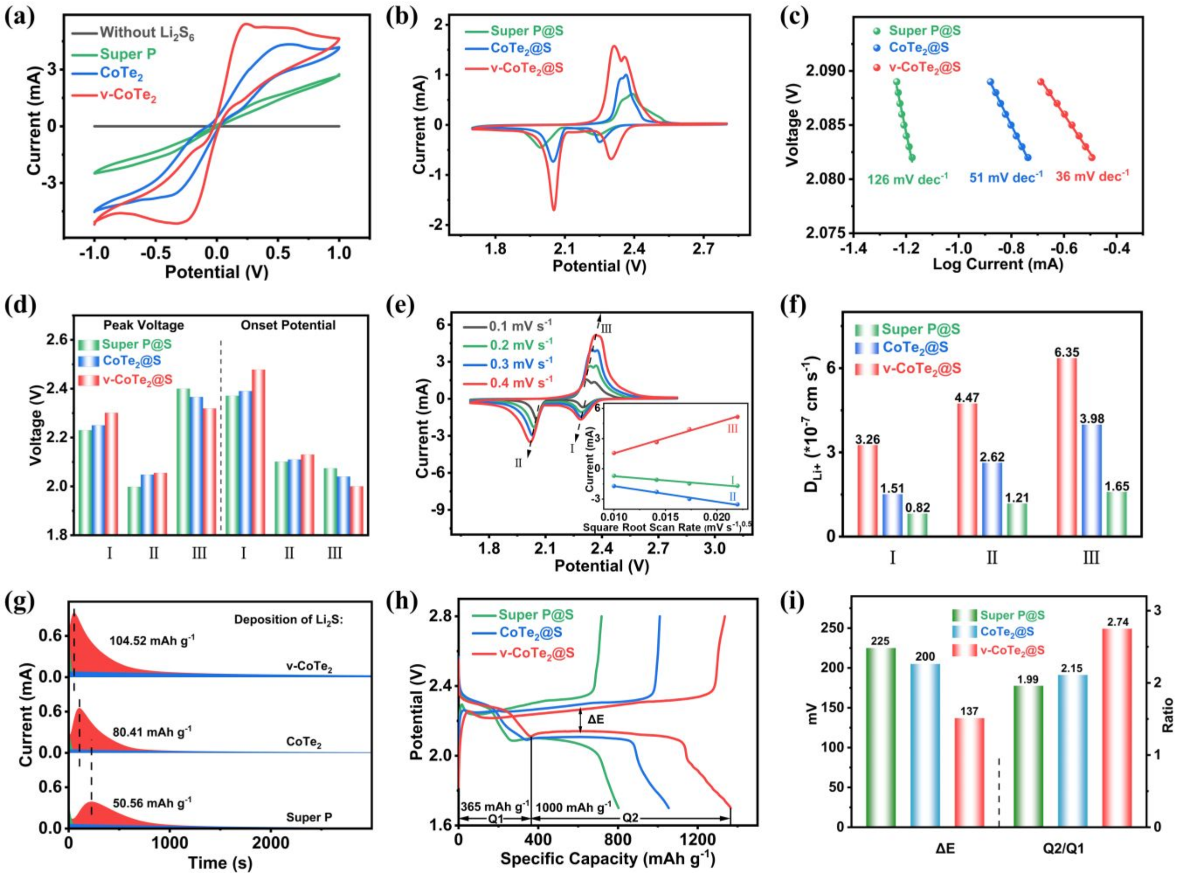

Figure 4. (a) CV curves of the symmetrical cells with various electrodes. (b) CV curves of LSBs with different electrodes at 0.1 mV s^{-1}. (c) Tafel slopes of coin cells equipped with v-$CoTe_2$@S, $CoTe_2$@S or Super P@S as electrode. (d) Peak voltages and onset potentials of different cathodes. (e) CV curves of v-$CoTe_2$@S cathode at different scan rates. (f) Li^+ diffusion coefficient calculated from the different CV redox peaks (peak I, peak II and peak III). (g) Potentiostatic discharge curves of Li_2S deposited on different catalyst surfaces. (h) Galvanostatic charge/discharge profiles of different electrodes at 0.1 C. (i) The values of ΔE and Q2/Q1 obtained from the charge/discharge curves.

The capacity ratio of the first discharge plateaus (Q1) and the second plateaus (Q2) provides an idea of the material catalytic activity for LiPS conversion. Q1 is the capacity of the reduction of S_8 to the soluble polysulfides, providing 4 electrons of the 16 electrons associated with the full S_8 lithiation process. Q2 is the capacity related to the further discharge to Li_2S and involves the other 12 electrons. The theoretical ratio of Q1/Q2 is 3. Because the reaction is rarely fully completed and some short-chain polysulfides may be lost in the process, experimentally Q1/Q2 is always below 3 and its value determines the reaction effectiveness. The Q1/Q2 values of all cathode materials are shown in Figure 4i. The v-$CoTe_2$ cathode exhibits the highest Q1/Q2 value at 2.74, well above the value obtained from $CoTe_2$ (2.15) and Super P (1.99). The high Q1/Q2 value obtained from v-$CoTe_2$ indicates an improved catalytic activity.

The facilitated redox kinetics of v-$CoTe_2$ was consistent with lower measured overpotentials for phase transformation between LiPS speccies and insoluble Li_2S_2/Li_2S during discharge/charge (Figure S16a and b) process.[14] The GCD curve of v-$CoTe_2$@S at different current densities are displayed in Figure 5a. The charge/dischaegr plateau were well maintained even at a high current rate of 3 C. In contrast, the discharge plateaus almost dissapeared for $CoTe_2$@S and Super P@S at 3 C (Figure S17). The rate performance of three materials are presented in Figure 5b and S18. The v-$CoTe_2$@S electrode exhibits superb rate performance with the highest specific capacities: 1365, 1050, 980, 912, 780, and 660 mAh g^{-1} from 0.1 C to 3 C, respectively. When the current density was returned to 0.5 C, the capacity of the v-$CoTe_2$@S electrode was recovered to 960 mAh g^{-1}, demonstrating excellent stability and reversibility.

The cycling stability of the three cathodes was evaluated at 1 C (Figure 5c). The coin cell with a v-$CoTe_2$@S cathode displayed a high initial discharge capacity of 812, and 89.9% of the initial capacity 729 mAh g^{-1} was still retained after 200 cycles. The Coulombic efficiency (CE) of the cell with v-$CoTe_2$@S cathode was above 99%, indicating the shuttle effect was effectively inhibited. Besides, the $CoTe_2$@S and Super P@S cathodes retained 393 and 220 mAh g^{-1} after 200 cycles, respectively (60.6% and 44.6% retention). These results further demonstrate the presence of $CoTe_2$ and particularly Te vacancies within this material not only enhance the sulfur utilization but also alleviates the shuttle effect.

The interfacial charge transfer kinetics of the as-prepared cells was investigated by electrochemical impedance spectroscopy (EIS). The cell with v-$CoTe_2$ cathode exhibited the smallest semicircle diameter at the high-frequency region, assigned to charge transfer resistance (R_{ct}) (Figure S19).[16, 56] According to the fitting results, using the equivalent circuit dispalyed in the inset of Figure S19, the R_{ct} of v-$CoTe_2$ (15.5 Ω) was smaller than $CoTe_2$ (32.3 Ω) and Super P (50.8 Ω). The corresponding EIS spectroscopy after cycling is presented in Figure 5d. No additional R-C element appears in the equivalent circuit (inset of Figure 5d), but lower R_{ct} were obtained for the three active materials due to the activation, S redistribution and improved electrolyte wetting of the composite during cycling. After cycling, the v-$CoTe_2$-based cell still showed the smallest Rct (6.5 Ω) compared with $CoTe_2$ (10.2 Ω) and Super P (30.5 Ω), indicating the fastest polysulfide conversion reaction and charge transfer kinetics.

Even at a high current rate of 3 C (Figure 5e), v-$CoTe_2$@S cathodes exhibit an excellent initial specific capacity and long-term cycle stability (0.039% decay per cycle), and a CE maintained above 99%, superior than that of $CoTe_2$@S and Super P@S. On the other hand, as a reference, a pure v-$CoTe_2$ cathode (without sulfur) was also tested, showing a negligible capacity when cycled under the same electrochemical conditions, thus proving no contribution of a potential redox of the telluride compound in the capacity (Figure S20).

For post-mortem studies on the cells, they were disassembled after 200 cycles at 1 C. The lithium metal foil of the v-$CoTe_2$@S coin cells showed lower corrosion and sulfur signals than those of $CoTe_2$@S and Super P@S, as shown in Figure S21. These results indicated the improved LiPS shuttling suppression capability of v-$CoTe_2$. Figure S22 shows the SEM images of the v-$CoTe_2$@S cathodes displaying the v-$CoTe_2$ polyhedron particles covered with a homogeneous Li_2S layer after full discharge, indicating both an excellent catalytic activity and structural stability as the porous v-$CoTe_2$ particle morphology maintained during lithiation/delithiation processes. On the other hand, the morphology of Cote changed from rhombic dodecahedron to irregular particles after cycling.

The evaluation of the performance of the host material under a high sulfur loading and a minimized amount of electrolyte is key to determining the practical application of the resulting LSBs. The performance of v-$CoTe_2$@S cathodes at a higher sulfur loading of 4.5 mg cm^{-2} (electrolyte/sulfur ratio (E/S) = 6 μL mg^{-1}) is displayed in Figure 5f. A stable areal capacity of 5.4 mAh cm^{-2} at 0.1 C was obtained after 50 cycles. Even when the sulfur content increases to 6.7 mg cm^{-2}, the cell with the v-$CoTe_2$@S cathode still exhibited a preeminent areal capacity of 6.1 mAh cm^{-2} after 50 cycles, which is significantly above that of commercial Li-ion batteries. The practicality of the assembled coin cell was subsequently verified by powering an electric fan (Figure 5g). Besides a v-$CoTe_2$@S-based pouch cell was assembled and demonstrated to power a LED strip (Figure S23). Figure 5h displays a comparison of the v-$CoTe_2$ with other sulfur host materials reported recently, demonstrating superior areal capacity and tiny decay rate per cycle (Figure 5h).[13, 57-59]

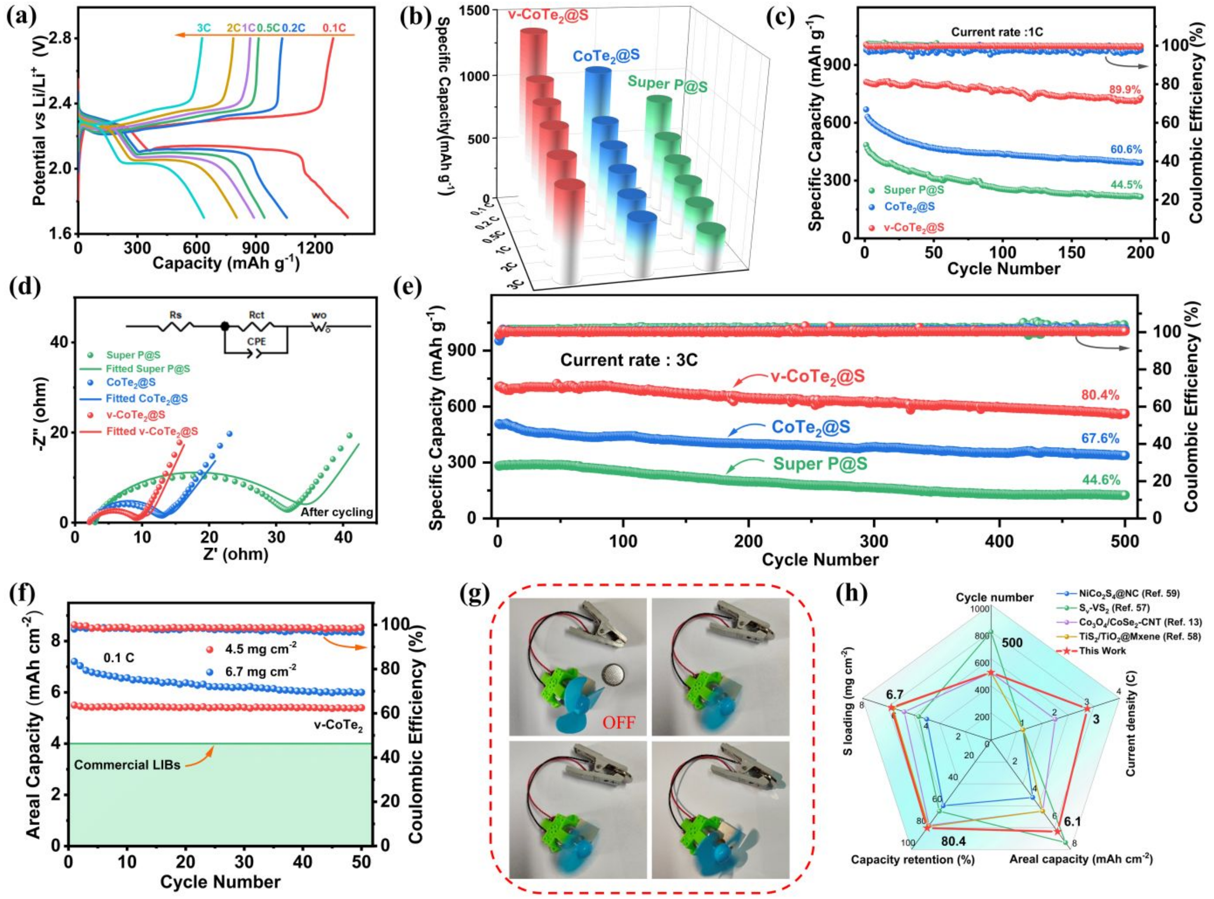

Figure 5. (a) GCD profiles of v-CoTe$_2$@S from 0.1 C to 3 C. (b) Rate performance of different cathodes. (c) Cycling life of v-CoTe$_2$@S, v-CoTe$_2$@S and Super P@S cathodes at 1 C. (d) EIS plot of three cathodes after cycling. (e) Cycling performances of three cathodes at of 3 C for 500 cycles. (f) Cycle performance of v-CoTe$_2$@S under high sulfur loadings and lean electrolyte conditions at 0.1 C. (g) Optical picture of electric fan powered by one v-CoTe$_2$ coin cell. (h) Comparison of the electrochemical performances of LSBs with v-CoTe$_2$@S electrodes with other published works.

To further understand the role of v-CoTe$_2$ in alleviating the shuttle effect of LiPS, *in situ* Raman spectroscopy was used. The Raman signal was obtained from the side of the lithium ring to reduce the disturbance of CoTe$_2$ (see details in the SI).[60] Figure 6a-d exhibits the *in situ* Raman spectra of coin cells based on v-CoTe$_2$ and CoTe$_2$ at 0.1 C in the discharge process. It is noteworthy that three Raman characteristic peaks (located at 152, 217, and 476 cm^{-1}) emerge at the beginning of the discharge process (≈ 2.31 V) and are associated with S_8^{2-}.[61] Additionally, the slight signal at 398 cm^{-1} in the $CoTe_2$ cell corresponds to S_6^{2-}, and indicates a partial sulfur conversion into LiPS at the initial stage of discharge. This may be due to the self-discharge during the standing time.[62] Continuing the discharge, the Raman peak of Li_2S_8 gradually vanishes at the second discharge platform (≈ 2.10 V). Raman characteristic peaks at 398 cm^{-1} begin to emerge and gradually increase to a maximum at 2.1 V, indicating a huge amount of Li_2S_6 has left the $CoTe_2$@S cathode due to severe shuttling behavior. As the discharge continues, the peaks at 456 cm^{-1} gradually increase until the discharge process is completed (≈ 1.7 V), correspond to Li_2S_4 + Li_2S_5. The existence of S_5^{2-} and S_4^{2-} illustrates the convesion of long-chain LiPS to short-chain LiPS.[63, 64] Overall, the $CoTe_2$@S cathode consistently show the peaks of LiPS throughout the entire discharge process, evidencing the severe shuttle effect in $CoTe_2$@S cell. On the contrary, only weak Raman signals can be detected from the contour plot of the v-$CoTe_2$@S cell throughout the entire discharge process. This comparison of the *in situ* Raman spectra confirms that the presence of Te vacancies within the porous $CoTe_2$ effectively alleviate the migration of polysulfide to the surface of anode during cycling as a result of an improved adsorption and enhanced electrocatalytic conversion.[20] Overall, the superior adsoption capacity and catalytic activity of v-$CoTe_2$ for the conversion of polysulfides is schematically shown in Figure 6e.

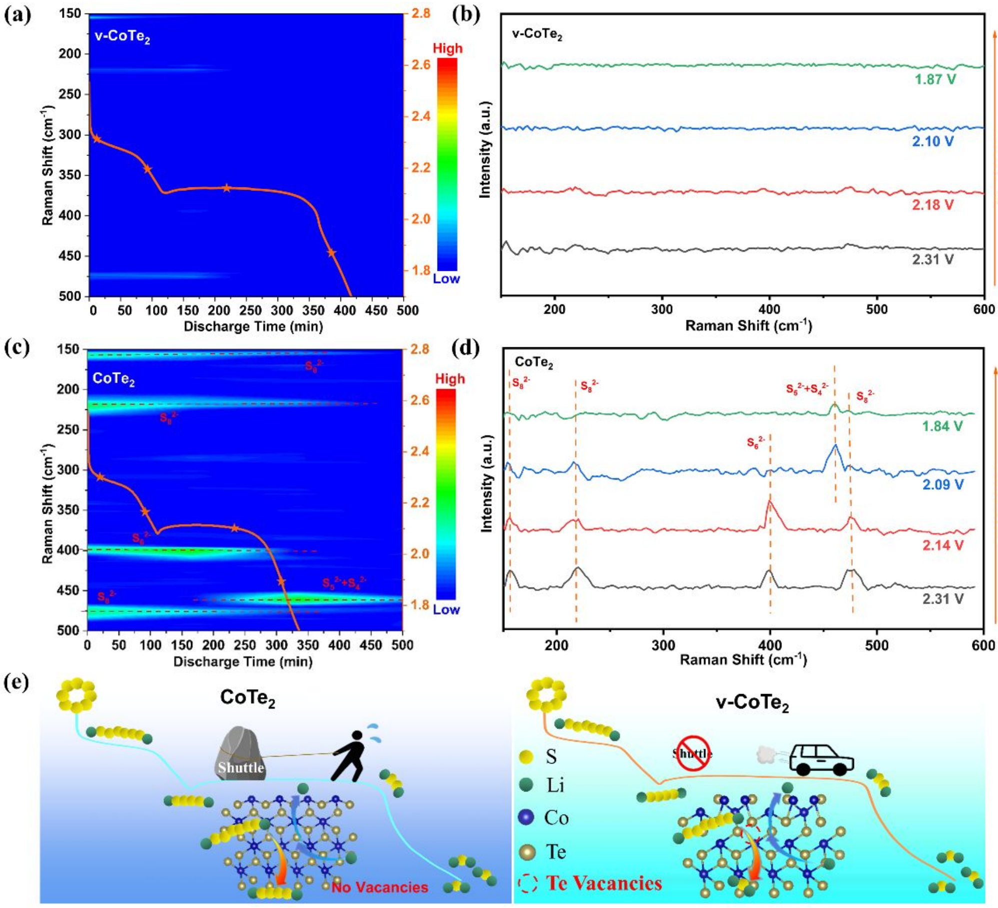

Figure 6. (a, c) *In situ* Raman spectra. (b, d) Raman spectra at different discharge voltages with the cells based on v-$CoTe_2$@S and $CoTe_2$@S cathodes. (e) Schematic of sulfur species trapping and conversion on v-$CoTe_2$ and $CoTe_2$ hosts.

Conclusions

In summary, we designed and prepared an efficient electrocatalyst using vacancy-defected $CoTe_2$ (v-$CoTe_2$) nanoparticles within a carbon framework as a sulfur host for LSBs. DFT calculations validated that v-$CoTe_2$ presents surface reconstruction around the surface vacancies of Te sites, exposing more Te atoms directly on the surface. This results in a robust multi-site coordination interaction between v-$CoTe_2$ and polysulfides like Li_2S_4, enhancing adsorption and preventing polysulfide migration from cathode to anode, thereby reducing active material loss. Additionally, the strong interaction facilitated by Te vacancies not only provides high adsorption energy but also accelerates polysulfide decomposition by weakening the S-S bond, thus promoting the redox conversion of LiPS. The experimental results are supported by DFT calculations, demonstrating v-$CoTe_2$'s superior catalytic activity compared to $CoTe_2$. Cells based on v-$CoTe_2$@S cathodes exhibit stable performance, retaining 80.4% capacity after 500 cycles at 3 C, with an average capacity decay of 0.039% per cycle. Even at a higher sulfur loading of 6.7 mg cm^{-2}, after 50 cycles, v-$CoTe_2$@S cathodes maintain a commendable areal capacity of 6.1 mAh cm^{-2}. This work underscores the potential of defect engineering as an effective strategy for optimizing the electrochemical performances of LSBs cathode materials.

Experimental Section

Chemicals: Cobalt(II) nitrate hexahydrate (analytical reagent, AR, $Co(NO_3)_2\cdot 6H_2O$), 2-methylimidazole (AR, $C_4H_6N_2$), tellurium powder (AR, Te), and methanol (AR, CH_3OH) were obtained from Adamas. Polyvinylidene fluoride (PVDF), N-methylpyrrolidone (NMP), 1,3-dioxolane (DOL) and 1,2-dimethoxyethane (DME) were purchased from Canrd. All chemicals were used as received, without further processing.

Synthesis of Co-ZIF-67: 5.82g cobalt(II) nitrate hexahydrate was dissolved in 150 mL of methanol, and 6.16g 2-methylimidazole was dissolved in another 150 mL methanol, representing solution A and solution B, respectively. Solution A was added to solution B with stirring and continued to stir for 24h at room temperature. The precipitate was then centrifuged with methanol and dried overnight.

Synthesis of v-$CoTe_2$: The obtained powder and tellurium powder were placed on the downstream and upstream of the furnace in a mass ratio of 1:3. The products was annealed at

600 °C in Ar atmosphere for 3h. The v-$CoTe_2$ powders were obtained by annealing at 350 °C for another 3h in Ar/H_2 atmosphere, while $CoTe_2$ requires no additional annealing.

Synthesis of v-$CoTe_2$@S, $CoTe_2$@S and Super P@S: The obtained v-$CoTe_2$ power was first grounded with sulfur at a mass ratio of 1:3 and heated at 155 °C for 12 h. $CoTe_2$@S and Super P@S were prepared in the same process as v-$CoTe_2$@S.

Synthesis of Li_2S_6 Solution and Adsorption Test: Sulfur and Li_2S were dissolved in same quantity of 1,2-dimethoxyethane (DME) and 3-dioxolane (DOL) with a molar ratio of 1:5, and then stirred overnight. v-$CoTe_2$, $CoTe_2$ and Super P (10mg) were immersed into 5 mL of 10×10^{-3} M Li_2S_6 solution overnight.

Supporting Information

The supporting information is available free of charge via the Internet at http://pubs.acs.org. The supporting information includes Figure S1-S23 and Table S1 as described in the text, specifically, additional SEM, TEM, XRD, TGA, CV, electrochemical performance, DFT simulation results, and crystal structure.

Corresponding Author

Email: dwyang@henu.edu.cn

Email: diaojf@utexas.edu

Email: zhangqiaobao@xmu.edu.cn

Email: acabot@irec.cat

ACKNOWLEDGMENTS

D. Yang thanks the funding from the National Natural Science Foundation of China (NSFC) (Grants No. 22305064). The authors thank the support from the project NANOGEN (PID2020-116093RB-C43), funded by MCIN/ AEI/10.13039/501100011033/ and by "ERDF A way of making Europe", by the "European Union". ICN2 acknowledges funding from Generalitat de Catalunya 2021SGR00457. This study is part of the Advanced Materials programme and was supported by MCIN with funding from European Union NextGenerationEU (PRTR-C17.I1) and by Generalitat de Catalunya. ICN2 is supported by the Severo Ochoa program from Spanish MCIN / AEI (Grant No.: CEX2021-001214-S) and is funded by the CERCA Programme / Generalitat de Catalunya. Q. Zhang thanks the Frontier Exploration Projects of Longmen Laboratory (grant no. LMQYTSKT008).

References

1. Bruce, P. G.; Freunberger, S. A.; Hardwick, L. J.; Tarascon, J.-M., Li–O_2 and Li–S batteries with high energy storage. *Nat. Mater.* **2012,** *11* (1), 19-29.
2. Zhou, G.; Wang, D.-W.; Li, F.; Hou, P.-X.; Yin, L.; Liu, C.; Lu, G. Q.; Gentle, I. R.; Cheng, H.-M., A flexible nanostructured sulphur–carbon nanotube cathode with high rate performance for Li-S batteries. *Energy Environ. Sci.* **2012,** *5* (10), 8901-8906.
3. Chou, S.-L.; Dou, S.-X., Next-Generation Batteries. *Adv. Mater.* **2017,** *29* (48), 1705871.
4. Manthiram, A.; Fu, Y.; Chung, S.-H.; Zu, C.; Su, Y.-S., Rechargeable Lithium–Sulfur Batteries. *Chem. Rev.* **2014,** *114* (23), 11751-11787.
5. Li, Z.; Wu, H. B.; Lou, X. W., Rational designs and engineering of hollow micro-/nanostructures as sulfur hosts for advanced lithium–sulfur batteries. *Energy Environ. Sci.* **2016,** *9* (10), 3061-3070.
6. Zhang, C.; Du, R.; Martí-Sánchez, S.; Xiao, K.; Yang, D.; Zhang, C.; Li, C.; Zeng, G.; Chang, X.; He, R.; Arbiol, J.; Li, J.; Jacas Biendicho, J.; Cabot, A. Tubular C_3N_4 Nanotubes as Metal-Free Sulfur Hosts toward Stable Lithium–Sulfur Batteries. *Energies* 2023, 16, 4545.
7. Yang, Y.; Zheng, G.; Cui, Y., Nanostructured sulfur cathodes. *Chem. Soc. Rev.* **2013,** *42* (7), 3018-3032.
8. He, J.; Luo, L.; Chen, Y.; Manthiram, A., Yolk–Shelled C@Fe_3O_4 Nanoboxes as Efficient Sulfur Hosts for High-Performance Lithium–Sulfur Batteries. *Adv. Mater.* **2017,** *29* (34), 1702707.
9. Yang, D.; Liang, Z.; Zhang, C.; Biendicho, J. J.; Botifoll, M.; Spadaro, M. C.; Chen, Q.; Li, M.; Ramon, A.; Moghaddam, A. O.; Llorca, J.; Wang, J.; Morante, J. R.; Arbiol, J.; Chou, S.-L.; Cabot, A., $NbSe_2$ Meets C_2N: A 2D-2D Heterostructure Catalysts as Multifunctional Polysulfide Mediator in Ultra-Long-Life Lithium–Sulfur Batteries. *Adv. Energy Mater.* **2021,** *11* (36), 2101250.
10. Zhang, J.; Li, Z.; Chen, Y.; Gao, S.; Lou, X. W., Nickel–Iron Layered Double Hydroxide Hollow Polyhedrons as a Superior Sulfur Host for Lithium–Sulfur Batteries. *Angew. Chem., Int. Ed.* **2018,** *57* (34), 10944-10948.

11. Yang, D.; Liang, Z.; Tang, P.; Zhang, C.; Tang, M.; Li, Q.; Biendicho, J. J.; Li, J.; Heggen, M.; Dunin-Borkowski, R. E.; Xu, M.; Llorca, J.; Arbiol, J.; Morante, J. R.; Chou, S.-L.; Cabot, A., A High Conductivity 1D π–d Conjugated Metal–Organic Framework with Efficient Polysulfide Trapping-Diffusion-Catalysis in Lithium–Sulfur Batteries. *Adv. Mater.* **2022,** *34* (10), 2108835.

12. Xia, L.; Wang, S.; Liu, G.; Ding, L.; Li, D.; Wang, H.; Qiao, S., Flexible SnO_2/N-Doped Carbon Nanofiber Films as Integrated Electrodes for Lithium-Ion Batteries with Superior Rate Capacity and Long Cycle Life. *Small* **2016,** *12* (7), 853-859.

13. Chu, R.; Nguyen, T. T.; Bai, Y.; Kim, N. H.; Lee, J. H., Uniformly Controlled Treble Boundary Using Enriched Adsorption Sites and Accelerated Catalyst Cathode for Robust Lithium–Sulfur Batteries. *Adv. Energy Mater.* **2022,** *12* (9), 2102805.

14. Zhang, C.; Du, R.; Biendicho, J. J.; Yi, M.; Xiao, K.; Yang, D.; Zhang, T.; Wang, X.; Arbiol, J.; Llorca, J.; Zhou, Y.; Morante, J. R.; Cabot, A., Tubular CoFeP@CN as a Mott–Schottky Catalyst with Multiple Adsorption Sites for Robust Lithium−Sulfur Batteries. *Adv. Energy Mater.* **2021,** *11* (24), 2100432.

15. Yang, D.; Li, M.; Zheng, X.; Han, X.; Zhang, C.; Jacas Biendicho, J.; Llorca, J.; Wang, J.; Hao, H.; Li, J.; Henkelman, G.; Arbiol, J.; Morante, J. R.; Mitlin, D.; Chou, S.; Cabot, A., Phase Engineering of Defective Copper Selenide toward Robust Lithium–Sulfur Batteries. *ACS Nano* **2022,** *16* (7), 11102-11114.

16. Yang, D.; Zhang, C.; Biendicho, J. J.; Han, X.; Liang, Z.; Du, R.; Li, M.; Li, J.; Arbiol, J.; Llorca, J.; Zhou, Y.; Morante, J. R.; Cabot, A., ZnSe/N-Doped Carbon Nanoreactor with Multiple Adsorption Sites for Stable Lithium–Sulfur Batteries. *ACS Nano* **2020,** *14* (11), 15492-15504.

17. Yang, D.; Li, C.; Sharma, M.; Li, M.; Wang, J.; Wei, J.; Liu, K.; Zhang, Y.; Li, J.; Henkelman, G.; Zhang, Q.; Cabot, A., Three birds with one arrow: Multifunctional single-atom catalysts enable efficient lithium-sulfur batteries. *Energy Storage Mater.* **2024,** *66*, 103240.

18. Liang, Z.; Yang, D.; Tang, P.; Zhang, C.; Jacas Biendicho, J.; Zhang, Y.; Llorca, J.; Wang, X.; Li, J.; Heggen, M.; David, J.; Dunin-Borkowski, R. E.; Zhou, Y.; Morante, J. R.; Cabot,

A.; Arbiol, J., Atomically dispersed Fe in a C_2N Based Catalyst as a Sulfur Host for Efficient Lithium–Sulfur Batteries. *Adv. Energy Mater.* **2021,** *11* (5), 2003507.

19. Xing, C.; Zhang, Y.; Xiao, K.; Han, X.; Liu, Y.; Nan, B.; Ramon, M. G.; Lim, K. H.; Li, J.; Arbiol, J.; Poudel, B.; Nozariasbmarz, A.; Li, W.; Ibáñez, M.; Cabot, A., Thermoelectric Performance of Surface-Engineered $Cu_{1.5-x}Te$–Cu_2Se Nanocomposites. *ACS Nano* **2023,** *17* (9), 8442-8452.
20. Yao, W.; Tian, C.; Yang, C.; Xu, J.; Meng, Y.; Manke, I.; Chen, N.; Wu, Z.; Zhan, L.; Wang, Y.; Chen, R., P-Doped $NiTe_2$ with Te-Vacancies in Lithium–Sulfur Batteries Prevents Shuttling and Promotes Polysulfide Conversion. *Adv. Mater.* **2022,** *34* (11), 2106370.
21. Zhang, C.; Fei, B.; Yang, D.; Zhan, H.; Wang, J.; Diao, J.; Li, J.; Henkelman, G.; Cai, D.; Biendicho, J. J.; Morante, J. R.; Cabot, A., Robust Lithium–Sulfur Batteries Enabled by Highly Conductive WSe_2-Based Superlattices with Tunable Interlayer Space. *Adv. Funct. Mater.* **2022,** *32*, 2201322.
22. Wang, B.; Wang, L.; Ding, D.; Zhai, Y.; Wang, F.; Jing, Z.; Yang, X.; Kong, Y.; Qian, Y.; Xu, L., Zinc-Assisted Cobalt Ditelluride Polyhedra Inducing Lattice Strain to Endow Efficient Adsorption-Catalysis for High-Energy Lithium–Sulfur Batteries. *Adv. Mater.* **2022,** *34* (50), 2204403.
23. Lao, Z.; Han, Z.; Ma, J.; Zhang, M.; Wu, X.; Jia, Y.; Gao, R.; Zhu, Y.; Xiao, X.; Yu, K.; Zhou, G., Band Structure Engineering and Orbital Orientation Control Constructing Dual Active Sites for Efficient Sulfur Redox Reaction. *Adv. Mater.* **2024,** *36* (2), 2309024.
24. Li, M.; Yang, D.; Biendicho, J. J.; Han, X.; Zhang, C.; Liu, K.; Diao, J.; Li, J.; Wang, J.; Heggen, M.; Dunin-Borkowski, R. E.; Wang, J.; Henkelman, G.; Morante, J. R.; Arbiol, J.; Chou, S.-L.; Cabot, A., Enhanced Polysulfide Conversion with Highly Conductive and Electrocatalytic Iodine-Doped Bismuth Selenide Nanosheets in Lithium–Sulfur Batteries. *Adv. Funct. Mater.* **2022,** *32* (26), 2200529.
25. Wang, J.; Zhao, Y.; Li, G.; Luo, D.; Liu, J.; Zhang, Y.; Wang, X.; Shui, L.; Chen, Z., Aligned sulfur-deficient ZnS_{1-x} nanotube arrays as efficient catalyzer for high-performance lithium/sulfur batteries. *Nano Energy* **2021,** *84*, 105891.

26. Zhang, Y.; Xing, C.; Liu, Y.; Spadaro, M. C.; Wang, X.; Li, M.; Xiao, K.; Zhang, T.; Guardia, P.; Lim, K. H.; Moghaddam, A. O.; Llorca, J.; Arbiol, J.; Ibáñez, M.; Cabot, A., Doping-mediated stabilization of copper vacancies to promote thermoelectric properties of $Cu_{2-x}S$. *Nano Energy* **2021,** *85*, 105991.

27. Hu, S.; Huang, X.; Zhang, L.; Li, G.; Chen, S.; Zhang, J.; Liu, X., Vacancy-Defect Topological Insulators Bi_2Te_{3-x} Embedded in N and B Co-Doped 1D Carbon Nanorods Using Ionic Liquid Dopants for Kinetics-Enhanced Li–S Batteries. *Adv. Funct. Mater.* **2023,** *33* (20), 2214161.

28. Huang, C.; Yu, J.; Zhang, C. Y.; Cui, Z.; Chen, J.; Lai, W.-H.; Lei, Y.-J.; Nan, B.; Lu, X.; He, R.; Gong, L.; Li, J.; Li, C.; Qi, X.; Xue, Q.; Zhou, J. Y.; Qi, X.; Balcells, L.; Arbiol, J.; Cabot, A., Electronic Spin Alignment within Homologous NiS_2/$NiSe_2$ Heterostructures to Promote Sulfur Redox Kinetics in Lithium-Sulfur Batteries. *Adv. Mater.* **2024,** *n/a* (n/a), 2400810.

29. Zhang, C. Y.; Gong, L.; Zhang, C.; Cheng, X.; Balcells, L.; Zeng, G.; Biendicho, J. J.; Li, J.; Sun, G. Z.; Zhou, J. Y.; Cabot, A., Sodium-Sulfur Batteries with Unprecedented Capacity, Cycling Stability and Operation Temperature Range Enabled by a $CoFe_2O_4$ Catalytic Additive Under an External Magnetic Field. *Adv. Funct. Mater.* **2023,** *33* (48), 2305908.

30. Zhang, C. Y.; Lu, X.; Han, X.; Yu, J.; Zhang, C.; Huang, C.; Balcells, L.; Manjón, A. G.; Jacas Biendicho, J.; Li, J.; Arbiol, J.; Sun, G.; Zhou, J. Y.; Cabot, A., Identifying the Role of the Cationic Geometric Configuration in Spinel Catalysts for Polysulfide Conversion in Sodium–Sulfur Batteries. *J. Am. Chem. Soc.* **2023,** *145* (34), 18992-19004.

31. Zhang, C. Y.; Zhang, C.; Sun, G. W.; Pan, J. L.; Gong, L.; Sun, G. Z.; Biendicho, J. J.; Balcells, L.; Fan, X. L.; Morante, J. R.; Zhou, J. Y.; Cabot, A., Spin Effect to Promote Reaction Kinetics and Overall Performance of Lithium-Sulfur Batteries under External Magnetic Field. *Angew. Chem., Int. Ed.* **2022,** *61* (49), e202211570.

32. Huang, C.; Yu, J.; Li, C.; Cui, Z.; Zhang, C.; Zhang, C.; Nan, B.; Li, J.; Arbiol, J.; Cabot, A., Combined Defect and Heterojunction Engineering in ZnTe/$CoTe_2$@NC Sulfur Hosts Toward Robust Lithium–Sulfur Batteries. *Adv. Funct. Mater.* **2023,** *33* (46), 2305624.

33. Zhou, X.; Jia, Z.; Zhang, X.; Wang, B.; Liu, X.; Xu, B.; Bi, L.; Wu, G., Electromagnetic

wave absorption performance of $NiCo_2X_4$ (X = O, S, Se, Te) spinel structures. *Chem. Eng. J.* **2021,** *420*, 129907.

34. Jiang, Y.; Wu, F.; Ye, Z.; Zhou, Y.; Chen, Y.; Zhang, Y.; lv, Z.; Li, L.; Xie, M.; Chen, R., Confining $CoTe_2$-ZnTe heterostructures on petal-like nitrogen-doped carbon for fast and robust sodium storage. *Chem. Eng. J.* **2023,** *451*, 138430.
35. Lin, J.; Wang, H.; Cao, J.; He, F.; Feng, J.; Qi, J., Engineering Se vacancies to promote the intrinsic activities of P doped $NiSe_2$ nanosheets for overall water splitting. *J. Colloid Interface Sci.* **2020,** *571*, 260-266.
36. Tian, Y.; Li, G.; Zhang, Y.; Luo, D.; Wang, X.; Zhao, Y.; Liu, H.; Ji, P.; Du, X.; Li, J.; Chen, Z., Low-Bandgap Se-Deficient Antimony Selenide as a Multifunctional Polysulfide Barrier toward High-Performance Lithium–Sulfur Batteries. *Adv. Mater.* **2020,** *32* (4), 1904876.
37. Yang, D.; Wang, J.; Lou, C.; Li, M.; Zhang, C.; Ramon, A.; Li, C.; Tang, M.; Henkelman, G.; Xu, M.; Li, J.; Llorca, J.; Arbiol, J.; Mitlin, D.; Zhou, G.; Cabot, A., Single-Atom Catalysts with Unsaturated $Co–N_2$ Active Sites Based on a C_2N 2D-Organic Framework for Efficient Sulfur Redox Reaction. *ACS Energy Lett.* **2024**, 2083-2091.
38. Xu, X.; Zhang, Y.; Sun, H.; Zhou, J.; Liu, Z.; Qiu, Z.; Wang, D.; Yang, C.; Zeng, Q.; Peng, Z.; Guo, S., Orthorhombic Cobalt Ditelluride with Te Vacancy Defects Anchoring on Elastic MXene Enables Efficient Potassium-Ion Storage. *Adv. Mater.* **2021,** *33* (31), 2100272.
39. Chen, Z.; Chen, M.; Yan, X.; Jia, H.; Fei, B.; Ha, Y.; Qing, H.; Yang, H.; Liu, M.; Wu, R., Vacancy Occupation-Driven Polymorphic Transformation in Cobalt Ditelluride for Boosted Oxygen Evolution Reaction. *ACS Nano* **2020,** *14* (6), 6968-6979.
40. Dong, C.; Liang, J.; He, Y.; Li, C.; Chen, X.; Guo, L.; Tian, F.; Qian, Y.; Xu, L., $NiS_{1.03}$ Hollow Spheres and Cages as Superhigh Rate Capacity and Stable Anode Materials for Half/Full Sodium-Ion Batteries. *ACS Nano* **2018,** *12* (8), 8277-8287.
41. Gaikwad, M. M.; Sarode, K. K.; Pathak, A. D.; Sharma, C. S., Ultrahigh rate and high-performance lithium-sulfur batteries with resorcinol-formaldehyde xerogel derived highly porous carbon matrix as sulfur cathode host. *Chem. Eng. J.* **2021,** *425*, 131521.

42. Bao, W.; Liu, L.; Wang, C.; Choi, S.; Wang, D.; Wang, G., Facile Synthesis of Crumpled Nitrogen-Doped MXene Nanosheets as a New Sulfur Host for Lithium–Sulfur Batteries. *Adv. Energy Mater.* **2018,** *8* (13), 1702485.
43. Song, Y.; Zou, L.; Wei, C.; Zhou, Y.; Hu, Y., Single-atom electrocatalysts for lithium–sulfur chemistry: Design principle, mechanism, and outlook. *Carbon Energy* **2023,** *5* (4), e286.
44. Pang, Q.; Tang, J.; Huang, H.; Liang, X.; Hart, C.; Tam, K. C.; Nazar, L. F., A Nitrogen and Sulfur Dual-Doped Carbon Derived from Polyrhodanine@Cellulose for Advanced Lithium–Sulfur Batteries. *Adv. Mater.* **2015,** *27* (39), 6021-6028.
45. Song, J.; Yu, Z.; Gordin, M. L.; Wang, D., Advanced Sulfur Cathode Enabled by Highly Crumpled Nitrogen-Doped Graphene Sheets for High-Energy-Density Lithium–Sulfur Batteries. *Nano Lett.* **2016,** *16* (2), 864-870.
46. Li, X.; Ding, K.; Gao, B.; Li, Q.; Li, Y.; Fu, J.; Zhang, X.; Chu, P. K.; Huo, K., Freestanding carbon encapsulated mesoporous vanadium nitride nanowires enable highly stable sulfur cathodes for lithium-sulfur batteries. *Nano Energy* **2017,** *40*, 655-662.
47. Li, H.; Shi, P.; Wang, L.; Yan, T.; Guo, T.; Xia, X.; Chen, C.; Mao, J.; Sun, D.; Zhang, L., Cooperative Catalysis of Polysulfides in Lithium-Sulfur Batteries through Adsorption Competition by Tuning Cationic Geometric Configuration of Dual-active Sites in Spinel Oxides. *Angew. Chem., Int. Ed.* **2023,** *62*, e202216286.
48. Pang, Q.; Kundu, D.; Cuisinier, M.; Nazar, L. F., Surface-enhanced redox chemistry of polysulphides on a metallic and polar host for lithium-sulphur batteries. *Nat. Commun.* **2014,** *5* (1), 4759.
49. Yang, D.; Han, Y.; Li, M.; Li, C.; Bi, W.; Gong, Q.; Zhang, J.; Zhang, J.; Zhou, Y.; Gao, H.; Arbiol, J.; Shi, Z.; Zhou, G.; Cabot, A., Highly Conductive Quasi-1D Hexagonal Chalcogenide Perovskite $Sr_8Ti_7S_{21}$ with Efficient Polysulfide Regulation in Lithium-Sulfur Batteries. *Adv. Funct. Mater.* **2024,** *n/a* (n/a), 2401577.
50. Du, Z.; Chen, X.; Hu, W.; Chuang, C.; Xie, S.; Hu, A.; Yan, W.; Kong, X.; Wu, X.; Ji, H.; Wan, L.-J., Cobalt in Nitrogen-Doped Graphene as Single-Atom Catalyst for High-Sulfur Content Lithium–Sulfur Batteries. *J. Am. Chem. Soc.* **2019,** *141* (9), 3977-3985.

51. Kong, L.; Li, B.-Q.; Peng, H.-J.; Zhang, R.; Xie, J.; Huang, J.-Q.; Zhang, Q., Porphyrin-Derived Graphene-Based Nanosheets Enabling Strong Polysulfide Chemisorption and Rapid Kinetics in Lithium–Sulfur Batteries. *Adv. Energy Mater.* **2018,** *8* (20), 1800849.

52. Yuan, B.; Hua, D.; Gu, X.; Shen, Y.; Xu, L.-C.; Li, X.; Zheng, B.; Wu, J.; Zhang, W.; Li, S.; Huo, F., Polar, catalytic, and conductive $CoSe_2$/C frameworks for performance enhanced S cathode in Li–S batteries. *J. Energy Chem.* **2020,** *48*, 128-135.

53. Zhu, X.; Zhao, W.; Song, Y.; Li, Q.; Ding, F.; Sun, J.; Zhang, L.; Liu, Z., In Situ Assembly of 2D Conductive Vanadium Disulfide with Graphene as a High-Sulfur-Loading Host for Lithium–Sulfur Batteries. *Adv. Energy Mater.* **2018,** *8* (20), 1800201.

54. Liu, Y.; Ying, Y.; Fei, L.; Liu, Y.; Hu, Q.; Zhang, G.; Pang, S. Y.; Lu, W.; Mak, C. L.; Luo, X.; Zhou, L.; Wei, M.; Huang, H., Valence Engineering via Selective Atomic Substitution on Tetrahedral Sites in Spinel Oxide for Highly Enhanced Oxygen Evolution Catalysis. *J. Am. Chem. Soc.* **2019,** *141*, 8136.

55. Zhou, G.; Tian, H.; Jin, Y.; Tao, X.; Liu, B.; Zhang, R.; Seh, Z. W.; Zhuo, D.; Liu, Y.; Sun, J.; Zhao, J.; Zu, C.; Wu, D. S.; Zhang, Q.; Cui, Y., Catalytic oxidation of Li_2S on the surface of metal sulfides for Li−S batteries. *Proc. Natl. Acad. Sci. U. S. A.* **2017,** *114* (5), 840-845.

56. Li, J.; Xu, X.; Yu, X.; Han, X.; Zhang, T.; Zuo, Y.; Zhang, C.; Yang, D.; Wang, X.; Luo, Z.; Arbiol, J.; Llorca, J.; Liu, J.; Cabot, A., Monodisperse CoSn and NiSn Nanoparticles Supported on Commercial Carbon as Anode for Lithium- and Potassium-Ion Batteries. *ACS Appl. Mater. Interfaces* **2020,** *12* (4), 4414-4422.

57. He, L.; Zhang, X.; Yang, D.; Li, J.; Wang, M.; Liu, S.; Qiu, J.; Ma, T.; Ba, J.; Wang, Y.; Wei, Y., Defect-Engineered VS_2 Electrocatalysts for Lithium–Sulfur Batteries. *Nano Lett.* **2023,** *23* (16), 7411-7418.

58. Nguyen, V. P.; Park, J. S.; Shim, H. C.; Yuk, J. M.; Kim, J.-H.; Kim, D.; Lee, S.-M., Accelerated Sulfur Evolution Reactions by TiS_2/TiO_2@MXene Host for High-Volumetric-Energy-Density Lithium–Sulfur Batteries. *Adv. Funct. Mater.* **2023,** *33* (35), 2303503.

59. Wu, Q.; Guo, T.; Wu, Z.; Shi, K.; Yang, X.; She, Z.; Zhao, R.; Ruan, Y., Boosting Polysulfide Transformation by $NiCo_2S_4$ Hollow Dodecahedra@Nitrogen-Doped Carbon Core/Shell Nanostructures as Cathodes for Lithium–Sulfur Batteries. *ACS Appl. Nano*

Mater. **2023,** *6* (9), 7456-7464.

60. Yu, B.; Huang, A.; Chen, D.; Srinivas, K.; Zhang, X.; Wang, X.; Wang, B.; Ma, F.; Liu, C.; Zhang, W.; He, J.; Wang, Z.; Chen, Y., In Situ Construction of Mo_2C Quantum Dots-Decorated CNT Networks as a Multifunctional Electrocatalyst for Advanced Lithium–Sulfur Batteries. *Small* **2021,** *17* (23), 2100460.
61. Chen, W.; Lei, T.; Qian, T.; Lv, W.; He, W.; Wu, C.; Liu, X.; Liu, J.; Chen, B.; Yan, C.; Xiong, J., A New Hydrophilic Binder Enabling Strongly Anchoring Polysulfides for High-Performance Sulfur Electrodes in Lithium-Sulfur Battery. *Adv. Energy Mater.* **2018,** *8* (12), 1702889.
62. Zhang, L.; Liu, Y.; Zhao, Z.; Jiang, P.; Zhang, T.; Li, M.; Pan, S.; Tang, T.; Wu, T.; Liu, P.; Hou, Y.; Lu,H., Enhanced Polysulfide Regulation via Porous Catalytic V_2O_3/V_8C_7 Heterostructures Derived from Metal–Organic Frameworks toward High-Performance Li–S Batteries. *ACS Nano* **2020,** *14* (7), 8495-8507.
63. Lei, T.; Chen, W.; Lv, W.; Huang, J.; Zhu, J.; Chu, J.; Yan, C.; Wu, C.; Yan, Y.; He, W.; Xiong, J.; Li, Y.; Yan, C.; Goodenough, J. B.; Duan, X., Inhibiting Polysulfide Shuttling with a Graphene Composite Separator for Highly Robust Lithium-Sulfur Batteries. *Joule* **2018,** *2* (10), 2091-2104.
64. Yao, W.; Zheng, W.; Xu, J.; Tian, C.; Han, K.; Sun, W.; Xiao, S., ZnS-SnS@NC Heterostructure as Robust Lithiophilicity and Sulfiphilicity Mediator toward High-Rate and Long-Life Lithium–Sulfur Batteries. *ACS Nano* **2021,** *15* (4), 7114-7130.

Abstract Graphics